# Influence of the Hydrogen Bonding Environment on Vibrational Coupling in the Electrical Double Layer at the Silica/Aqueous Interface

Shyam Parshotam, Benjamin Rehl, Franziska Busse, Alex Brown, and Julianne M. Gibbs[a]

[a]Department of Chemistry, University of Alberta, Edmonton, Alberta, T6G 2G2, Canada

Abstract

Vibrational spectroscopy is a powerful tool for determining the local hydrogen-bonding environment. However, vibrational coupling present in H_2O can make it difficult to relate vibrational spectra to a molecular description of the system. While numerous bulk studies have shed light on this phenomenon, the influence of both intra- and intermolecular vibrational coupling on the resulting electrical double layer spectra at buried interfaces remains largely unexplored. By utilizing the combination of vibrational sum frequency generation (vSFG), electrokinetic measurements, and the maximum entropy method on isotopically diluted water (HOD) at the silica/aqueous interface, we reveal the influence of vibrational coupling on the Stern and diffuse layer spectra as the surface charge density is varied. By comparing our HOD spectra with the corresponding H_2O spectra from pH 10 to 2, we find that the diffuse layer spectra of H_2O are dominated by both intra- and intermolecular coupling leading to significant differences in the H_2O and HOD spectra. In contrast, the spectral response of HOD and H_2O in the Stern layer as a function of pH is similar, providing strong evidence that the O-H oscillators in the Stern layer are evolving in a similar manner for both the H_2O and HOD systems. However, we observe differences in the frequency centers at low pH that are less significant at higher pH suggesting that intermolecular coupling in the Stern layer is evolving as the surface charge density is varied.
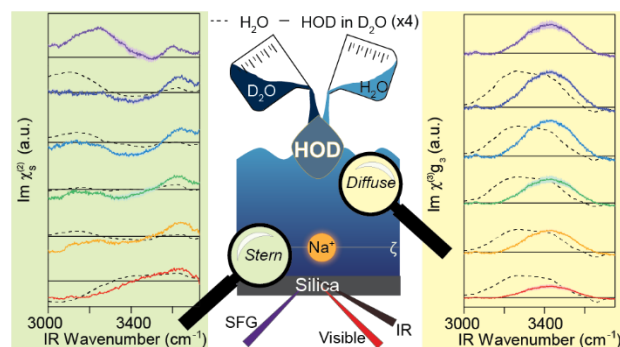
Introduction

The electrical double layer (EDL) represents a fundamental model of the interaction between a charged surface and the aqueous phase and accordingly is of central relevance to modeling both natural and engineered systems.[1] Information on the electrical double layer has been obtained using a wide variety of methods such as atomic force measurements (AFM),[2] X-ray spectroscopies using synchrotron light sources,[3,4] electrokinetic measurements,[5] and nonlinear optical techniques.[6,7] The underlying features determined from these measurements are strongly influenced by the sensitivity of the technique to the constituents of the EDL. For example, electrokinetic measurements give valuable information on the electric potential at the slipping plane of the EDL. However, the dominant constituent in the EDL is H_2O molecules, and their interactions with each other, ions, and the charged surface play critical roles in modulating the EDL structure and dynamics.

Vibrational sum frequency generation (vSFG) is an ideal technique to probe H_2O molecules in the EDL, as it is intrinsically sensitive to the number and order of the molecules at the surface allowing information such as the hydrogen bonding environment to be characterized.[6,8] However, for charged surfaces, such as the silica/H_2O interface, constructing a molecular picture is hindered by the presence of the electric field generated by the presence of charges due to

deprotonation of silanol groups at pH values above ~2,[9,10] which align bulk water molecules. As vSFG is sensitive to the entire EDL, it is difficult to determine the contributions of H_2O molecules near the surface (i.e., in the Stern,[11,12] bonded interfacial,[13–15] or topmost layer[16]) and those contributing further away in the diffuse layer.

Several strategies have been applied to access the Stern layer spectral contributions at aqueous mineral oxide interfaces, such as suppressing the diffuse layer by employing a gate-controlled semiconductor/oxide/water junction[15] or by raising the ionic strength.[16,17] Most relevant to this work, Wen et al.[14] presented a route for separating the diffuse layer spectrum from the total EDL spectrum for water molecules interacting with a Langmuir-Blodget film without diffuse layer suppression by taking the difference complex spectrum between two conditions with similar surface charge densities and accounting for changes in electric potential. By uncovering the diffuse layer complex spectrum, the imaginary component of the Stern layer complex spectrum could be predicted, which is primarily of interest when constructing a molecular description of the interface. In our previous work, we modified this approach by utilizing zeta (ζ) potentials from either streaming current or potential measurements in combination with the maximum entropy method to deconvolute the Stern and diffuse layer spectra as the ionic strength and pH were varied at the silica/H_2O interface.[11,18]

However, for the silica/H_2O interface, the Stern and diffuse layer spectra are intricately tied to the intra- and inter- molecular vibrational coupling of H_2O. Intramolecular coupling between the bending overtone with the fundamental O-H stretch mode leads to a Fermi resonance characterized by the 3200 cm^{-1} mode in the vSFG spectrum.[19–21] This Fermi resonance significantly complicates the spectral interpretation making it difficult to relate spectral changes to changes in the intermolecular resonant coupling (i.e. structural changes) between neighboring

H_2O molecules. Moreover, the strength of the hydrogen bonding interactions of the H_2O (manifested in the position of the resonant frequency) is also obscured. Both of these forms of coupling can be minimized by using isotopically diluted H_2O (HOD in D_2O).[22–24] Removing intramolecular coupling results in the absence of the Fermi resonance and hence its contribution to the spectrum at 3200 cm^{-1}. Meanwhile, the absence of intermolecular resonant coupling leads to the narrowing and blue shift of the OH stretch. [23,25]

Isotopically diluted H_2O has been extensively utilized in vSFG studies at several interfaces.[16,19–21,26–31] In particular, Tahara and co-workers[16] used it in their phase sensitive vSFG experiments where they suppressed the diffuse layer contribution by increasing the ionic strength up to 5 M at a single pH of 12 at the silica/H_2O and silica/HOD interfaces. This work allowed them to identify Stern and diffuse layer spectra (labeled as the $\chi^{(2)}_{\text{topmost}}$ and $\chi^{(2)}_{\text{EDL}}$ spectra, respectively) at pH 12. They found a remarkable similarity between the Stern layer spectra of HOD and H_2O at pH 12 and high ionic strength indicating that H_2O molecules at the silica interface were vibrationally decoupled under these conditions. However, owing to the nature of these experiments, the influence of the ions and pH on the EDL could not be deconvoluted although both are known to strongly influence the structure of H_2O in the EDL.[11,18,32–35] Furthermore, as we have shown previously, the structure of H_2O in the Stern layer changes significantly as the pH is lowered below 12.[18]

We now expand our previous studies at the silica/H_2O interface by studying the silica/HOD (HOD in D_2O) interface in a bid to uncover the role vibrational coupling plays in the H_2O spectra of the Stern layer over varied surface charge densities beyond the measurements reported in Urashima et al.[16] We achieve this by measuring the vSFG spectra and zeta potentials at the silica/HOD interface with varying pH at constant ionic strength and varying ionic strength at

constant pH. Using the maximum entropy method and Wen et al.'s approach we can deconvolute the responses of the Stern and diffuse layers. We find strong similarities in the Stern layer spectral shape between HOD and H_2O at the silica interface at all pH values. Yet as the pH is lowered from 10 to 2, the resonant frequencies of HOD in the Stern layer are blue shifted with respect to those observed for H_2O. These differences in the frequency centers suggest that intermolecular resonant coupling becomes prominent at lower pH values. The source of the coupling could potentially be the change in hydrogen bonding environment of H_2O from a singly hydrogen bond donating structure (asymmetric) to a doubly hydrogen bond donating structure with other H_2O molecules owing to a flip in the H_2O near the silica surface as the pH is lowered.

Experimental Section
Materials

IR-grade fused silica hemispheres (Almaz optics, KI, 1 inch diameter) were used for vSFG experiments. IR-grade fused silica windows (Almaz optics, KI, 2.5 inch diameter, 8 mm thickness) were used for zeta potential measurements. Silica substrates were cleaned with HPLC grade methanol (Fisher Chemical), sulfuric acid (95-98 %, Caledon Laboratories), and hydrogen peroxide (30 % w/w in H_2O, Sigma-Aldrich). Solutions were made with NaCl (99.99%, trace metal basis, Alfa Aesar), KCl (99.999%, trace metal basis, Acros Organics), NaOH (99.99%, trace metal basis, Sigma Aldrich), HCl (34-37%, trace metal grade, Fisher Chemicals). Ultrapure deionized H_2O (18.2 MΩcm) was used during all experiments. Deuterium oxide (99.9% D, Sigma Aldrich) was utilized in conjunction with H_2O in the ratio of 4:1 (D_2O: H_2O) to yield mixtures in the ratio of 1:8:16 (H_2O: HOD: D_2O).

Sample Preparation

Before vSFG or zeta potential measurements, silica substrates were rinsed and sonicated for 5 min each in deionized H_2O, HPLC grade methanol, and then with deionized H_2O again before being immersed in piranha solution (3:1 H_2SO_4:H_2O_2) for 1 hr. The substrate was rinsed and sonicated in the same manner as before followed by drying in an oven (>100°C) for 15 min. For vSFG experiments, an in-house Teflon sample cell was rinsed and sonicated in deionized H_2O, MeOH, and deionized H_2O. The cell was then allowed to sit open to the atmosphere. HOD solutions were prepared using a ratio of 1:4 (H_2O: D_2O). To convert the measured pH values of HOD in D_2O to pD values we add 0.32 to the measured pH. However, for convenience sake we refer to pD for D_2O as pH as we directly compare the pD and pH values between HOD in D_2O and H_2O, respectively.[21,36,37]

Caution: Piranha solution reacts violently with organic material. Ensure there is no residual methanol on the substrate before immersion in piranha.

Laser Assembly

A regeneratively amplified laser (Spectra-Physics, Spitfire Pro, 1 kHz, 94 fs, 3.3 W) was seeded and pumped by a Ti-sapphire oscillator (Spectra-Physics, MaiTai, 80 MHz) and Nd-YLF laser (Spectra-Physics, Empower 30), respectively, to generate 800 nm pulses. A 65% beam splitter (Newport) directed the 800-nm pulse to a noncollinear optical parametric amplifier (TOPAS-C/nDFG, Light Conversion) to produce tunable broadband IR pulses. The IR light was passed through a long pass filter (Edmund Optics, 2.40 m, 68-653), polarizer (Thorlabs), a zero-order, tunable half waveplate (Alphalas), and then a CaF_2 focusing lens (Thorlabs, f= 500 mm) focused the IR light to the sample. The remaining 800 nm light from the Spitfire Pro was passed through an air-spaced Fabry Perot Etalon (TecOptics), polarizer (Thorlabs), zero-order half

waveplate (Thorlabs), and then a focusing lens (Thorlabs, f=500 mm) which directs the light to the sample. Both the visible and IR beams were spatially and temporally overlapped at the sample interface to generate sum frequency (SF) light. The SF light went through a BK7 recollimating lens (Thorlabs, f = 400 mm), a half-wave plate (Thorlabs), a Glan-Thompson calcite polarizer (Thorlabs), a focusing lens (Thorlabs), and a filter (Thorlabs) before entering a spectrograph (Princeton Instruments, Acton SP-2556, 600 grooves/mm grating) connected to a thermoelectrically cooled (-75 °C) charge coupled device camera (Princeton Instruments, Acton PIXIS 100B CCD).

vSFG Experiments

The laser was aligned and optimized using the sum frequency light generated from the silica/gold interface. Following this process, eight IR pulses were collected at one delay setting to cover the range from 2800 to 3700 cm^{-1}. A polystyrene calibration film (International Crystal Laboratories) was utilized to calibrate the detected frequencies. The gold coated hemisphere was replaced with the cleaned silica hemisphere. Before any measurement, the cell was thoroughly rinsed with the solution to be measured. For pH titrations, each solution was allowed to equilibrate before the spectral acquisition. The order of the solutions was H_2O (30 mins equilibration), 10 mM NaCl/water, and 50 mM NaCl/HOD. The pH of the 50 mM NaCl/HOD solution was adjusted using NaOH to reach pH ~10 and HCl was used to titrate from pH 10 to 2. For measurements involving the variation of the ionic strength, an initial volume of HOD solution was placed into the clean cell. By adding specific volumes of concentrated NaCl stock solutions, the desired concentration was achieved. Spectra obtained were divided by that from the silica/gold interface which was utilized as the reference. To facilitate a comparison between H_2O and HOD, the (S-polarized SFG, S-polarized visible, and P-polarized IR) spectra were normalized to the 3200 cm^{-1}

mode intensity measurement at the silica/10 mM NaCl water interface. Details on the local field corrections are provided in the supporting information.

Zeta Potential Experiments

Electrokinetic measurements were performed on a SurPASS Electrokinetic Analyzer (Anton Paar) using a clamping cell with spacers and sealing foil. The conductivity probe (Anton Paar, 18116) and pH probe (Anton Paar) were calibrated with 0.1 M KCl solution, and pH 4, 7, and 10 buffer solutions before every experiment. Prior to the clamping cell being mounted, the instrument was cleaned with deionized H_2O 5 times (300 s for each cleaning cycle). The clamping cell was mounted with two fused silica windows, with one of the plates with 2 holes to allow a channel to be formed between the 2 fused silica windows. The instrument was filled with deionized H_2O (200s) and a flow check was performed (500 mBar) to ensure no leakages in the channel. The instrument was then rinsed with deionized H_2O (500 mBar for 500 s), allowed to equilibrate for at least 30 mins, and the zeta potential of H_2O is determined. The H_2O was then removed, and air passed through the instrument several times. HOD was then passed through the instrument with similar equilibration times as H_2O. Higher salt concentrations were used to dilute the HOD to obtain the zeta potential as a function of the ionic strength. Measurements were performed under streaming current mode with rinse pressure of 500 mBar for 180s and ramp pressure of 400 mBar for 20s. For the pH titration, 50 mM NaCl/HOD solution was allowed to equilibrate, the pH was adjusted to 10 with NaOH diluted in 50mM HOD, and then HCl was used to adjust the pH of the solution. The zeta potential was determined using the Helmholtz-Smoluchowski equation given by

$$\zeta = \frac{dI}{dP} \times \frac{\eta}{\varepsilon_o \varepsilon} \times \frac{L}{A}. \qquad \qquad \textbf{Equation 1}$$

where $\frac{dI}{dP}$ denotes the streaming current, η is the viscosity, ε is the dielectric constant, L is the length of the channel, and A is the area.[38]

To account for the differences in the viscosity and dielectric constant between HOD and H_2O, the values of 0.99 mPas and 78.23 were used for HOD while 0.89 mPas and 78.4 were used for H_2O.[39–41] A weighted average of D_2O and H_2O was used for HOD at 25°C.

Maximum Entropy Method Analysis

A more detailed version of the maximum entropy method (MEM) analysis can be found in previous vSFG work.[42–44] In brief, the maximum entropy method approximates the complex spectra from the intensity spectra. The spectral entropy, h, is given by

$$h \propto \int_0^1 log I(v) dv .$$ **Equation 2**

where $I(v)$ is the intensity spectrum and v is the rescaled frequency range from 0 to 1. Constraining the entropy to maximum and forbidding the growth of resonances over time, Lagrange multipliers give

$$I(v) = \frac{|b|^2}{\left|1+\sum_{m=1}^{M} a_m e^{i2\pi mv}\right|^2} .$$ **Equation 3**

where the coefficients a_m and b can be determined from the Toeplitz system of equations for 2M+1 data points. The Toeplitz system of equations is

$$\begin{bmatrix} R(0) & \cdots & R(-M) \\ \vdots & \ddots & \vdots \\ R(M) & \cdots & R(0) \end{bmatrix} \begin{pmatrix} 1 \\ a_1 \\ \vdots \\ a_M \end{pmatrix} = \begin{pmatrix} |b|^2 \\ 0 \\ \vdots \\ 0 \end{pmatrix} .$$ **Equation 4**

where $R(m)$ is the autocorrelation function given by

$$R(m) = \int_0^1 I(v)e^{-i2\pi mv} \, dv \, .$$ **Equation 5**

The complex-valued $\chi^{(2)}$ can be determined by

$$\chi^{(2)}(v) = \frac{be^{i\varphi(v)}}{1+\sum_{m=1}^{M} a_m e^{i2\pi mv}} \, .$$ **Equation 6**

In Eq. (6), the numerator is the frequency dependent error phase, while the inverse of the denominator is the MEM complex spectrum. The unknown error phase is required to determine the actual phase (i.e., $\chi^{(2)}$ phase) of the vSFG spectrum ($\varphi(v)$) from the MEM phase, whereby

$$\chi^{(2)} \, phase \, = \, Error \, phase \, + \, MEM \, phase.$$ **Equation 7**

Result and Discussion
## Homodyne vSFG and Zeta Potentials

Broadband vibrational sum frequency generation (vSFG) involves the spatial and temporal overlap of a broadband IR light field and a narrow visible light field, which generates an intensity spectrum at the sum of the incident field frequencies. Owing to resonant enhancement, the spectra are sensitive to the molecules with vibrational modes that are vSFG active and excited by the incident IR.[45] Moreover, within the electric dipole approximation these molecules must be assembled non-centrosymmetrically to contribute to vSFG. The observed changes in the intensity of the sum frequency light can be described by the following equation:

$$I_{SF} \propto \left| \chi_{total}^{(2)} \right|^2 = \left| \chi_s^{(2)} + \chi^{(3)} g_3 \right|^2.$$ **Equation 8**

Here $\chi_s^{(2)}$ is the second-order susceptibility that reports on molecules in the Stern layer,[13] and $\chi^{(3)}$ is the third-order nonlinear susceptibility which describes the SFG response of water in a bulk-like environment. The value of g_3 is determined from the interfacial potential, which we

approximate by the zeta potential, and accounts for optical interference in the diffuse layer that occurs at low ionic strength.[46,47] This $\chi^{(3)}g_3$ term represents the contribution of H_2O or HOD molecules aligned or polarized by the interfacial potential, which is analogous to the diffuse layer component of the EDL.

To evaluate the vSFG responses of HOD and H_2O at the silica interface, we measured the SSP (S-polarized SFG, S-polarized visible, and P-polarized IR) and PPP intensity spectra in the O-H stretching region as the pH was varied and in the presence of 50 mM NaCl (Fig 1). Changing the pH alters the surface charge density of silica since the surface silanol groups are weak acids and become deprotonated as the pH is raised above 2, which is in the range of the point of zero charge of silica.[10] Changing the protonation state of the surface silanol sites should manifest in changes to both the Stern layer ($\chi_s^{(2)}$) and diffuse layer ($\chi^{(3)}g_3$) spectra. For example, in our previous work with H_2O at a constant ionic strength (50 mM NaCl), as the silica surface became less charged with decreasing pH from 10 to 2, the hydrogen bonding environment of the H_2O in the Stern layer evolved significantly, while the diffuse layer contribution decreased with the decreasing magnitude of the interfacial potential (g_3 term in eq 8).[11]
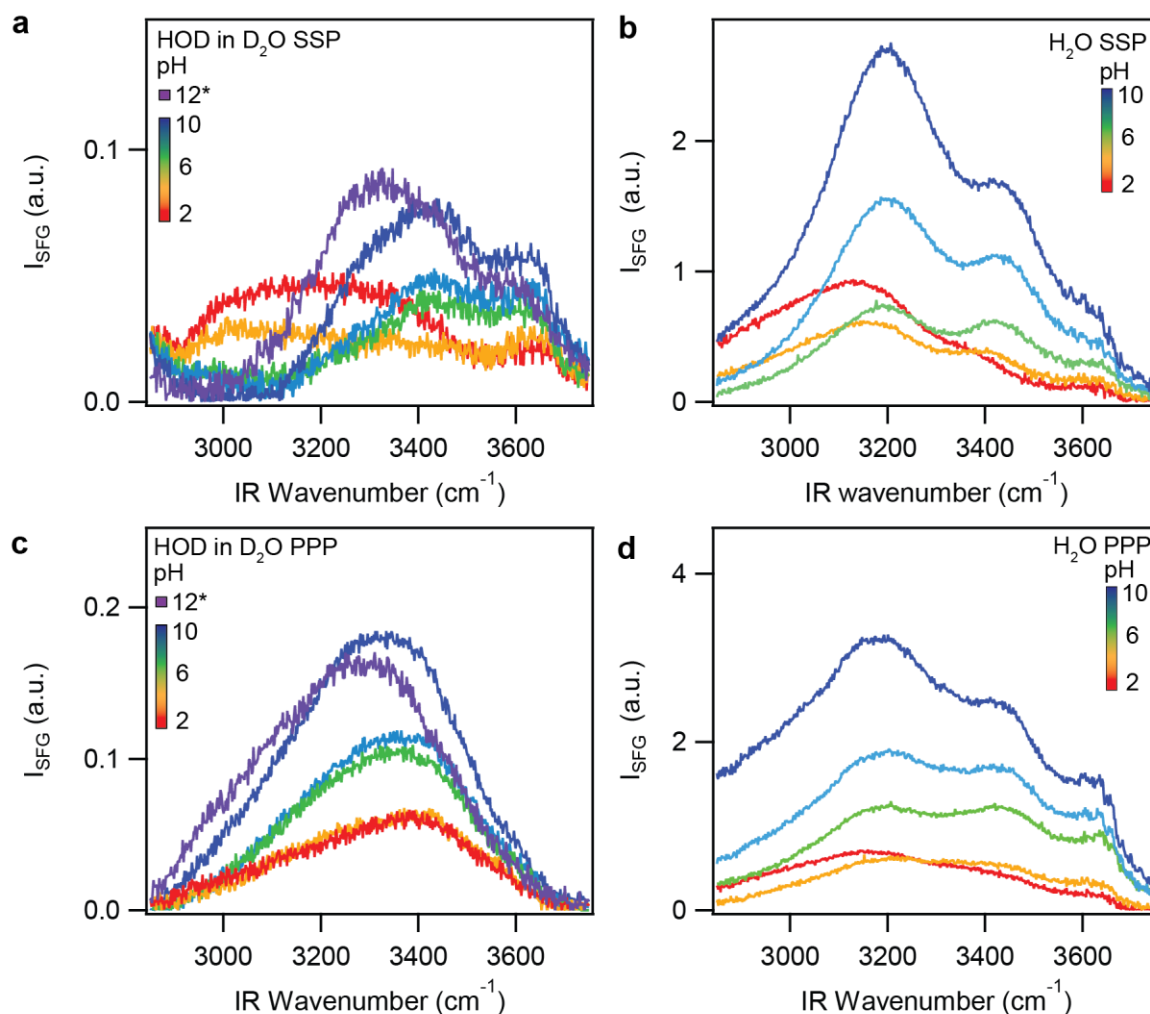
Figure 1. Representative SSP vSFG intensity spectra corrected for local field effects from 2850 to 3750 cm^{-1} at the (a) silica/HOD and (b) silica/H$_2$O interfaces[11] as the pH was varied from 10 to 2 with under a 50 mM NaCl background electrolyte. Representative PPP vSFG intensity spectra without local field corrections at the (c) silica/HOD and (d) silica/H$_2$O interfaces. To allow for comparison to previous work,[16] we also separately measured the SSP and PPP spectra at the pH 12 silica/HOD interface.

Consistent with previous work,[21] the SSP intensity spectra of the silica/HOD interface at natural pH (~pH 7 based on equilibrium with atmospheric CO$_2$) and 50 mM NaCl exhibited a broad peak at 3400 cm^{-1}, a narrower peak at 3600 cm^{-1}, and the tail of another mode below 3000 cm^{-1}. As the pH was decreased from pH 10 to pH 2, the 3400 cm^{-1} and 3600 cm^{-1} modes began to decrease while a new 3200 cm^{-1} mode increased in intensity, becoming most prominent at pH 2.

In contrast, the SSP spectra of silica/H_2O exhibited a feature in the intensity spectra at 3200 cm^{-1} over the entire pH range (Fig 1b).[11] Although there is expected to be a broad distribution of hydrogen-bonding environments at this hydrophilic interface,[20] the 3200 cm^{-1} mode for the H_2O spectra contains significant contributions from the Fermi resonance.[19] Yet the evolution of the spectral shape of H_2O based on variations in intensity of the 3200 and 3400 cm^{-1} modes have been analyzed in previous work to obtain information on the interfacial structure of H_2O.[17,34,35,48]

The PPP spectra of the silica/HOD interface presented in Fig 1c display a vastly different spectral line shape and response to alterations in the pH than that of the SSP spectra. In this polarization combination, one symmetric broad peak centered at ~3300 cm^{-1} dominated the spectra at pH 10 and gradually became blue-shifted and asymmetric as the pH decreased. In a separate experiment we measured the spectrum at pH 12, for comparison with previous work[49] and found the spectral position was the most red-shifted at pH 12 consistent with the trend observed from pH 10 to 2. The variations observed at low pH in the SSP spectral shape did not appear in the PPP spectra as the pH was varied. This strong dependence on the polarization combination is in stark contrast to the SSP and PPP spectral shape from the silica/H_2O interface, presented in Fig 1b and 1d, respectively, that exhibit the 3200 cm^{-1}, 3400 cm^{-1}, and 3600 cm^{-1} modes consistently throughout the pH range as well as the red-shift at low pH.

The difference between the polarization combinations for the HOD system is further exemplified by a comparison of the square root of the integrated area of the intensity spectra (proportional to $\chi^{(2)}_{total}$) and the corresponding zeta potentials, which were determined for the same type of planar silica sample under the same experimental conditions (Fig 2). As shown in Fig 2a, the PPP and SSP integrated areas of silica/HOD exhibit different pH dependent trends: the integrated area of the PPP spectra following the zeta potentials more closely than that from the

SSP spectra where the former is more monotonic than the latter. Meanwhile, for the silica/H_2O system displayed in Fig 2b, the integrated area exhibits a similar non-monotonic response for both PPP and SSP integrated areas over the pH range. We attribute this similarity between the PPP and SSP spectra and their pH-dependence to the contribution of the Fermi resonance to the diffuse layer spectra for the H_2O system, which contributes significantly to the spectral response at lower wavenumber (vide infra).
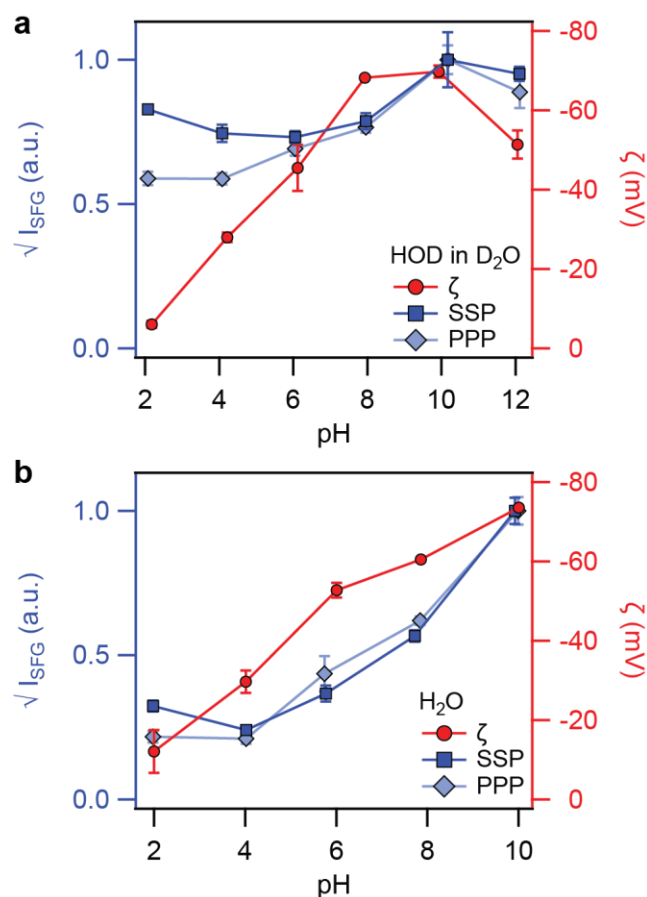
Figure 2. The square root of the average values of the integrated SSP (local field-corrected) and PPP spectra from 2850 to 3750 cm^{-1} (blue), normalized to the value at pH 10, and the corresponding zeta potentials, ζ, (red) at the (a) silica/HOD and (b) silica/H_2O[11] interfaces collected from pH 10 to 2 with a background of 50 mM NaCl. Error bars are the standard deviation from replicate measurements.

To determine the diffuse layer component of the complex spectra, we rely on our reported methodology to determine the $\chi^{(3)}$ spectrum of HOD.[11,18] This methodology requires measuring the zeta potentials and the vSFG spectra as the ionic strength is varied at a constant pH. We present the vSFG spectra as the ionic strength was varied at the silica/HOD interface at natural pH in Fig 3a. While the variation in the pH led to prominent shifts in the peak positions in the SSP spectra (Fig 1), particularly for the HOD interface, the influence of varying the ionic strength was less pronounced in both the H_2O and HOD spectra. Likewise, minimal changes in peak positions were observed in the PPP spectra (Fig S2). For both systems, the effect of increasing the ionic strength was most apparent in the intensities of the spectra. As the ionic strength was increased in H_2O or HOD in D_2O equilibrated with atmospheric CO_2, we observed an initial growth in intensity followed by a decrease in the SSP spectra in both systems. Such a trend has been previously reported and attributed to changes in optical interference within the diffuse layer as the ionic-strength dependent Debye length approaches the coherence length followed by charge screening at higher salt concentrations.[18,46,50,51]
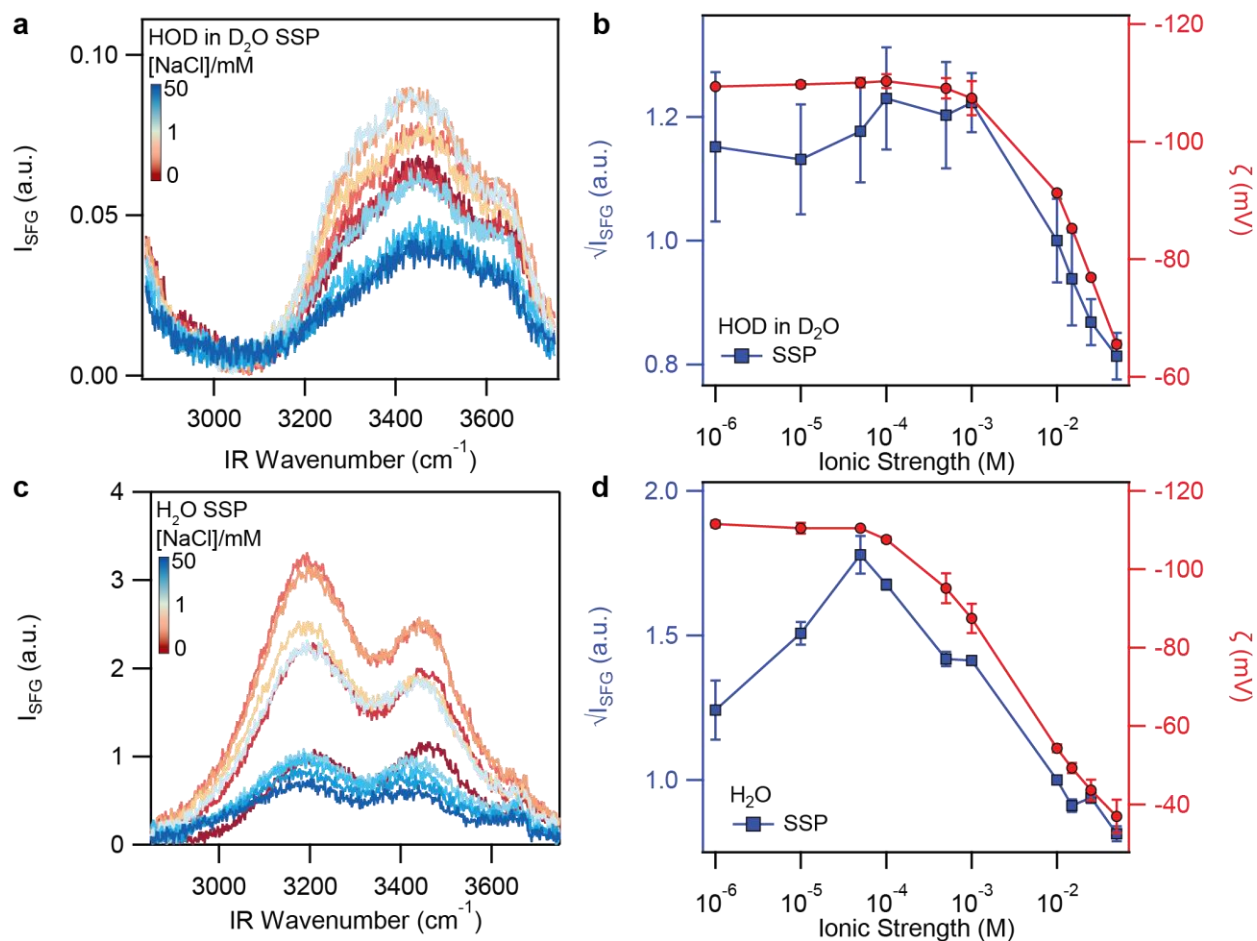
Figure 3. Representative SSP vSFG intensity spectra corrected for local field effects from 2850 to 3750 cm^{-1} and accompanying average square root of the integrated spectral areas (blue squares) and average zeta potentials (red circles) at the (a-b) silica/HOD and (c-d) silica/H$_2$O interfaces collected from the neat (no added salt) solution to an ionic strength of 50 mM NaCl. Error bars are from the standard deviation of replicate measurements.

However, there is a difference in the salt-dependent trends of HOD and H$_2$O. For the silica/H$_2$O interface, the maximum intensity was observed at 0.01 mM NaCl, whereas for the HOD system, the maximum was observed for an ionic strength of 0.1 mM. This is also notable in the evolution of the corresponding zeta potential with ionic strength. Indeed, by computing the electrokinetic charge densities predicted by the Grahame equation,[52] we observed differences in the charge densities between HOD and H$_2$O with added salt (Fig S3). These differences warrant

further investigations as previous work comparing D_2O and H_2O have found intrinsic variations between the species.[53]

Complex vSFG Spectra of HOD

Thus far, we have compared the intensity spectra ($\left|\chi_{total}^{(2)}\right|^2$) of the two interfaces. However, to deconvolute the contributions of the Stern ($\chi_s^{(2)}$) and diffuse ($\chi^{(3)}g_3$) layers from the overall intensity spectra, we need to determine the complex spectra, which we and others[13,14] refer to as $\chi_{total}^{(2)}$. To obtain the SSP complex spectra from the intensity spectra presented in Figures 1 and 3, we employ the maximum entropy method (MEM), which has been previously utilized in several vSFG studies.[42–44,54–60] We attribute the rising intensity at lower wavenumber (<3000 cm^{-1}) in the SSP intensity spectra of HOD to the tail of the O-D stretch from D_2O. Therefore, to avoid any interferences from the O-D region, we truncate our spectra at 3000 cm^{-1} in the following analysis.

The MEM estimates the complex spectra from the intensity spectra by identifying the most probable phase under the constraint of maximizing spectral entropy and assuming no growth of resonances over time. The outcome of the analysis is the MEM complex spectra that can be separated into the amplitude and the 'MEM phase,' which is related to the actual phase (i.e., the $\chi^{(2)}$ phase) of the spectra (φ) by the so-called error phase as shown in equation 7. In our previous work at the silica/neat H_2O interface,[11,18] we made use of the phase-sensitive vSFG measurements by Myalitsin et al.[21] to predict the error phase under specific conditions. Heterodyne second harmonic generation (HD-SHG)[61,62] was then used to predict changes in the error phase with varying pH or ionic strength conditions that were not previously acquired by phase sensitive vSFG

measurements. Under all these various conditions, the error phase remained linear with respect to the wavenumber.

For the HOD system, we followed the same methodology to use the intensities and complex spectra presented by Myalitsin et al.[21] to determine the error phases at pH 2.1, 7.2, 12.1 and ionic strength of 10 mM phosphate buffer solution (PBS) as shown in Fig 4a (bold lines). Using MEM analysis of our intensity spectra and the error phase spectra from their data, our resulting imaginary spectra at pH 2 and pH 12 were in good agreement with their phase-sensitive vSFG measurements (Fig 4b). Here the amplitude difference at pH 12 relative to pH 2 is likely due to the higher ionic strength in our system. However, we found that the error phase of HOD determined from Myalitsin et al.[21] is nonlinear with respect to wavenumber at pH 7 and is highly sensitive to variations in the pH. Furthermore, a shift in the error phase from HOD at natural pH with no added salt (which we estimate to be at pH 7.5) to pH 7 HOD (and 10 mM PBS) makes it difficult to decipher the influence of ions on the error phase (Fig S4). Therefore, we required new procedures to predict the error phase as the pH and ionic strength were varied.

For the experiments performed with varying pH and a background of 50 mM NaCl, we interpolated the error phase derived from the phase-sensitive vSFG measurements at pH 2.1, 7.2, and 12.1.[21] As shown by the dashed lines in Fig 4a, this approach assumed for simplicity that the error phase with respect to each wavenumber varies linearly with the pH. The resultant complex spectra utilizing the interpolated error phases with the MEM analysis of our intensity spectra as the pH is varied are shown in Fig 4c. The sign of the modes in the resulting imaginary spectra reflects the orientation of the O-H oscillators within the EDL.[63] Specifically, for the OH oscillators, the positive sign indicates that the oscillator is pointing with dipole moment (i.e., hydrogen atom) towards the surface, while a negative sign represents the opposite direction. The variation in the

imaginary spectra of HOD mimics that of H_2O as at low pH there is a transition from negative to positive amplitude of the imaginary component of $\chi^{(2)}$ in the lower wavenumber region.[11,21]
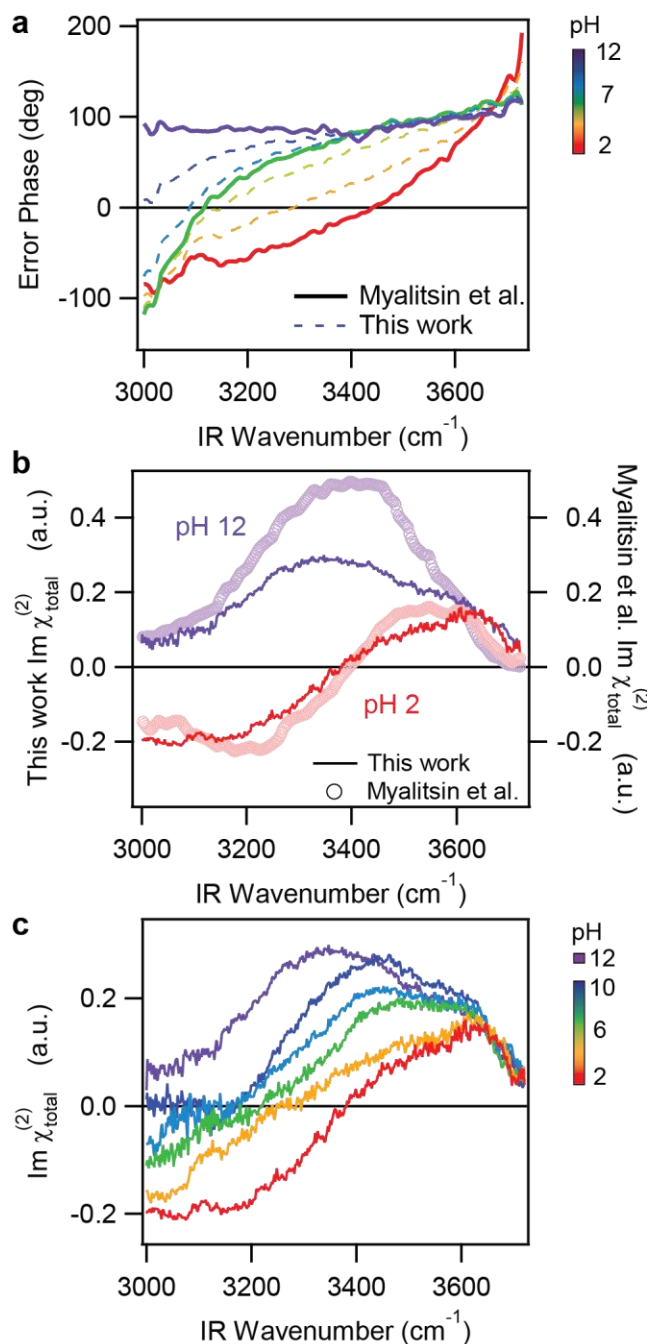

Figure 4. (a) Interpolation of the error phase extracted from Myalitsin et al.[21] as the pH is varied. (b) Comparison of the imaginary $\chi^{(2)}_{total}$ spectra at pH 2 and pH 12 measured by Myalitsin et al.[21] and determined by maximum entropy method analysis of our intensity spectra. (c) The imaginary

$\chi_{\text{total}}^{(2)}$ spectra using the interpolated error phases and MEM analysis of our intensity spectra presented in Fig 1a.

While the interpolation of the error phase shown above can be used to predict the complex spectra with varying pH and constant ionic strength, we cannot use this approach to predict the influence of increasing the ionic strength on the error phase as reference complex spectra have only been reported at two different ionic strengths (neat and 10 mM PBS), which do not adequately cover the range explored in our experiments (neat to 50 mM). However, for both the phase-sensitive vSFG measurements at the silica/HOD interface with 10 mM PBS (pH 7) and neat HOD, we find that the $\chi^{(2)}$ phase (φ) is linear between 3000 and 3700 cm^{-1} (Fig 5a). Furthermore, we observed for both reference spectra and their corresponding MEM analysis that there were three points where the φ phase could be predicted. Two of the points were when the MEM phase intersected the x-axis (i.e., MEM phase = 0). According to equation 8, at these points, the φ phase is equal to the error phase, which we found was approximately 90° (-90° at low wavenumber and +90° at high wavenumber) as shown in Fig S5. The last point is where the slope of the MEM phase changed sign, which was observed to correspond to the point at which the φ phase was zero in these reference spectra. Therefore, we utilized the same relationship between our MEM phase and φ phase for the spectra at natural pH with increasing ionic strength to 50 mM. The $\chi^{(2)}$ phase (φ) at an ionic strength of 10 mM predicted from our MEM phase spectrum is shown in Fig 5a (red line), which shows excellent agreement with the φ spectrum measured by Myalitsin et al.[21] (peach line). The error phase spectra determined accordingly for each NaCl concentration are shown in Fig S7.

The complex spectra at an ionic strength of 10 mM determined from this method of analysis are in good agreement with the phase-sensitive vSFG measurements as presented in Fig 5b. The

imaginary component of the complex spectra over the ionic strength range studied are presented

in Fig 5c with the accompanying real spectra presented in the supplementary material.

a

b

c
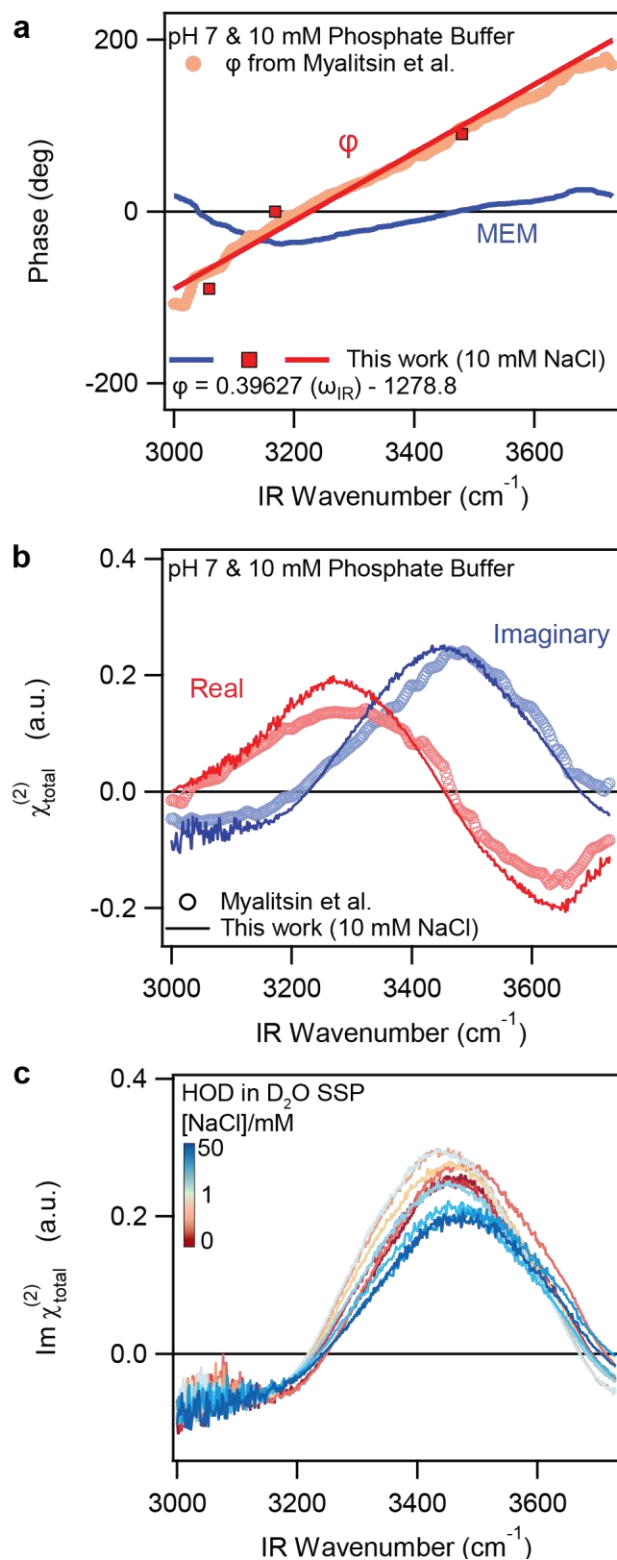
Figure 5. (a) The $\chi^{(2)}$ phase (φ) determined from the reference complex spectrum of Myalitsin et al.[21] (peach line) and that determined from the MEM phase of our measured intensity spectrum (red squares). The linear fit of the three data points (red squares) was used as the wavenumber-dependent error phase in our analysis for this set of experimental conditions. (b) The real (red) and imaginary (blue) spectra of 10 mM NaCl HOD at natural pH, which are similar to the HD-SFG measurements of the silica/HOD interface with 10 mM phosphate buffer at pH 7. (c) Imaginary spectra over the ionic strength range of neat HOD to 50 mM NaCl using the calculated frequency-dependent error phase for each salt concentration and MEM analysis of the corresponding intensity spectra.

Stern and Diffuse Layer Spectra

With the complex $\chi^{(2)}_{\text{total}}$ spectra in hand, we can now proceed to the deconvolution of the Stern and diffuse layer spectra. To achieve this goal, we followed the route proposed by Wen et al.,[14] which we have used in our previous work at the silica/H$_2$O interface.[11,18] The analysis entailed determination of the $\chi^{(3)}$ term by finding two different ionic strength points where we assumed the Stern layer ($\chi^{(2)}_s$) structure was unchanging and that all differences between the spectra were due to differences in g_3 (for further details about determining the $\chi^{(3)}$ spectrum see supporting information). The resultant complex $\chi^{(3)}$ obtained from this analysis is presented in Fig 6.
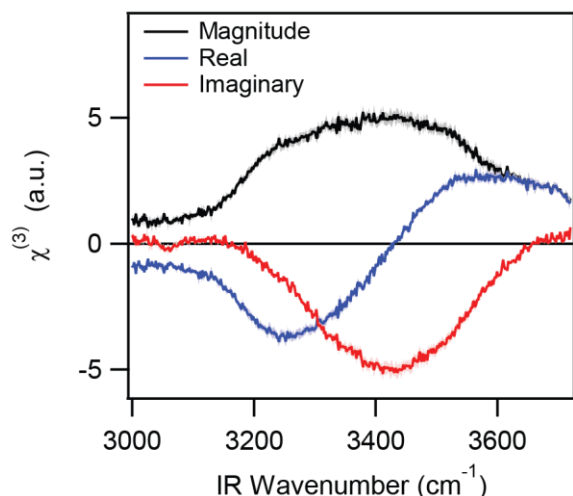
Figure 6. The complex $\chi^{(3)}$ spectrum of the silica/HOD interface. The reported complex spectrum is the average from analyzing replicate SFG measurements. Shaded areas represent the error bars propagated from the zeta potential measurements.

To test our $\chi^{(3)}$ spectrum, we determined the resulting $\chi^{(3)}g_3$ (diffuse layer) spectrum at pH 12 with a background of 50 mM NaCl and compared it to that from Urashima et al.[16] (Fig 7a and Fig S9a) who based it on the overall difference spectra at high salt concentration (~100 mM and 1 M). Our diffuse layer spectra is similar to that reported by Urashima et al.[16] as both of the spectra depict a single peak centered at ~3400 cm^{-1}. As further support of our $\chi^{(3)}$ spectrum, we determined the Stern layer imaginary spectrum for the silica/HOD interface at pH 12 and 50 mM NaCl and found a strong resemblance to the analogous $\chi^{(2)}_{\text{topmost}}$ spectrum of Urashima et al.[16] (Fig 7b and Fig S9b), with slight line shape deviations at extreme high (>3600 cm^{-1}) and low (<3100 cm^{-1}) wavenumbers being the major difference (vide infra). Nonetheless, our Stern layer line shape at pH 12 and 50 mM NaCl bears striking similarity to that measured by Urashima et al.[16] at pH 12 and 2 M.

With confidence in our $\chi^{(3)}$ spectrum of HOD, we determined the pH dependent diffuse layer spectra of HOD by multiplying the corresponding g_3 values with $\chi^{(3)}$ and made a comparison to that reported for the interface with H_2O (Fig 7a).[11,18] Similar to infrared and Raman studies, the vSFG spectral response of H_2O is red shifted with respect to that of the isotopically diluted water (HOD), which is attributed to the intermolecular resonant coupling present in H_2O.[16] Additionally, the difference in spectral line shape and the lack of amplitude at lower wavenumber for the HOD compared with H_2O suggest that the Fermi resonance contributes significantly to the latter. Nevertheless both $\chi^{(3)}$ spectral responses are dominated by a negative mode in the imaginary spectra, with a small positive feature above 3600 cm^{-1}. Furthermore, the intensity of H_2O versus HOD in the diffuse layer spectra (Fig 7a) is consistent with the lesser amount of OH oscillators in the latter (made by diluting 1 part H_2O in 4 parts D_2O). Additionally, we note that there is a strong similarity of the diffuse layer HOD imaginary spectra to the PPP intensity spectra

from HOD (Fig 1c) suggesting that the PPP spectra of HOD are picking up more contributions from the diffuse layer (the $\chi^{(3)}g_3$ term) than the SSP spectra.
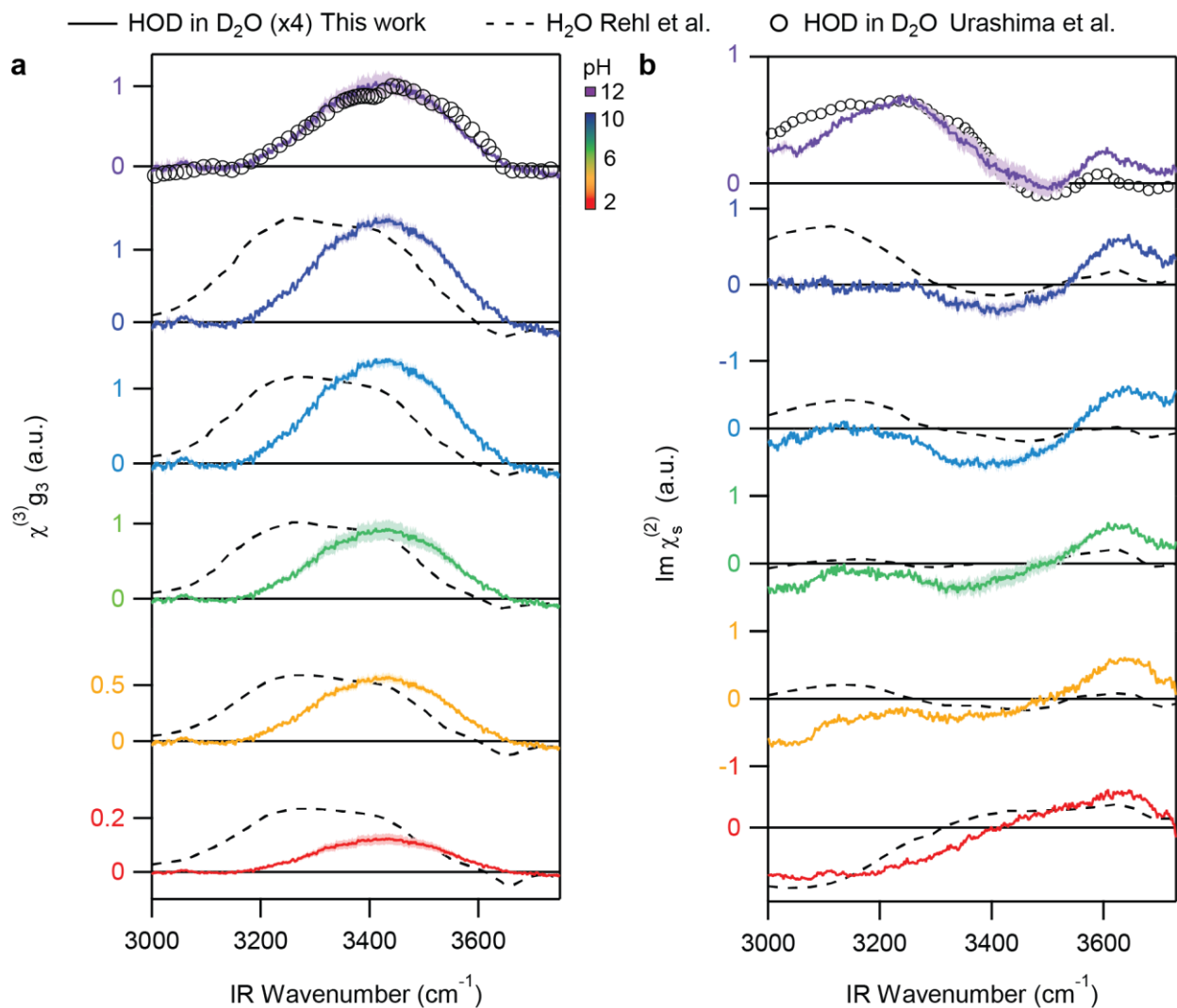

Figure 7. (a) Stern layer ($\chi_s^{(2)}$) and (b) diffuse layer ($\chi^{(3)}g_3$) spectra of HOD and H_2O over the pH range of 10 to 2 at 50 mM NaCl. The H_2O spectra were reported in our previous work (Rehl et al.[11]). Additional measurement at pH 12 are also included to allow for comparison with rescaled measurements at pH 12 and 2 M by Urashima et al.[16] Shaded areas represent the uncertainty propagated from the zeta potential measurements.

To determine the Stern layer spectra, the $\chi^{(3)}g_3$ spectra were subtracted from the corresponding $\chi_{total}^{(2)}$ complex spectra. Even though the diffuse layer spectra exhibit a significant difference, the overall spectral shape in the Stern layer of HOD shows a striking resemblance to

that of H_2O with subtle differences as shown in Fig 7a. In our previous work, we identified the three spectral regions associated with the different types of hydrogen bonding environments of H_2O in the Stern layer.[11,18] Accordingly, we assign the positive feature at 3150 cm^{-1} to O-H oscillators that donate hydrogen bonds to the negative siloxide surface sites. For both H_2O and HOD, as the pH is decreased from 10 to 4 this low wavenumber mode decreases in magnitude. This new negative mode at 3150 cm^{-1} is attributed to H_2O accepting hydrogen bonds from the neutral silanol sites as the surface becomes less negatively charged approaching the point-of-zero charge at pH 2. The positive mode at 3400 cm^{-1}, seen most clearly in the H_2O Stern layer spectra at pH 2, was attributed to hydrogen-bond donation to neutral sites. As the pH was lowered, this region shifted from negative to positive for the silica/HOD interface, but the overall contribution to the spectra is quite weak and therefore we hesitate to draw conclusions regarding the change to the surface structure. The mode above 3600 cm^{-1} in both sets of spectra which did change significantly with pH has been assigned by some to the OH from a silanol site, which they also found was pH insensitive.[65,66]

There are marginal differences in the spectral shape of the Stern layer imaginary spectra for the HOD and H_2O systems as the surface charge density is varied. Specifically, at pH 2, a distinct red shift and broader response can be observed in the negative 3150 cm^{-1} mode in the Stern layer spectrum of H_2O compared with that of HOD. However, as the pH is increased the differences between the peak positions or pH where the spectra cross through zero converge. Above pH 6, the deprotonation of silanol sites results in a flip of the O-H oscillators of the surface-bound HOD that contribute at low wavenumber, now with hydrogens directed towards the silica surface, presumably at siloxide sites (SiO$^-$). This hydrogen bonding interaction for the OH oscillator in both H_2O and HOD that donate a hydrogen to SiO$^-$ would in principle be the same if

the H_2O is decoupled owing to interactions with the surface. This conclusion is consistent with that put forth by Urashima et al.[16] who found that the spectral shape of HOD and H_2O in the Stern layer was very similar at pH 12 indicating that HOD and H_2O are in similar environments as the surface becomes negatively charged.

In contrast at pH 2, the O-H oscillators that contribute at 3150 cm^{-1} point in the direction of the bulk solution (i.e., hydrogens pointed away from the surface). This orientation corresponds to the H_2O (or HOD) acting as a hydrogen bond acceptor for silanol sites and as hydrogen bond donor to H_2O (or D_2O) molecules. A red shift and broadening in the peak positions in the vibrational spectra have been related to the presence of intermolecular resonant coupling present in H_2O as a result of hydrogen bonding with H_2O molecules.[23,25] Furthermore, previous molecular dynamics simulations at the air/water interface have shown that the type of hydrogen bonding structure regulates the intermolecular resonant coupling.[67,68] In their simulations, symmetric double donor hydrogen bonding environments contribute more significantly to intermolecular resonant coupling as compared to asymmetric single donor hydrogen bonding environments. As such we propose that below pH 6, the hydrogen bonding structure of water in the Stern layer exhibits contributions of intermolecular resonant coupling. As a result, a double donor hydrogen bonding structure is promoted giving rise to the red shift in the Stern layer spectrum of H_2O compared with that of HOD. At higher pH values, these differences notably become less prominent as the oscillators begin to shift to an asymmetric hydrogen bonding environment thereby decoupling the O-H oscillators of water. This highlights the influence of the surface charge density on both the hydrogen bonding network and vibrational coupling at the silica/water interface.

Conclusions

In summary, by utilizing vSFG in combination with the maximum entropy method and electrokinetic measurements at the silica/HOD interface and comparing it with our previous work at the silica/H_2O interface,[11] we can elucidate the spectral response of vibrational coupling in different parts of the electric double layer. Over the pH range of 10 to 2, vSFG intensity spectra of H_2O and HOD at the silica interface exhibit different spectral responses due to the absence of the Fermi resonance in the HOD spectra. Furthermore, the silica/HOD interface displayed different spectral line shapes in PPP and SSP polarization combinations. By employing the maximum entropy method on the SSP intensity spectra and electrokinetic measurements, we extracted the Stern ($\chi_s^{(2)}$) and diffuse layer ($\chi^{(3)}g_3$) spectra over the pH range. The similarity in the Stern and diffuse complex spectral signatures to the phase-sensitive measurements of Urashima et al.[16] at pH 12 highlights the reliability of our approach. The difference in the diffuse layer spectral shape of H_2O and HOD, marked by the notable absence of the 3200 cm^{-1} mode in the latter, is due to the absence of intramolecular coupling (Fermi resonance) and the red shift of the H_2O spectra due to intermolecular resonant coupling. On the other hand, the spectra in the Stern layer are qualitatively like that of H_2O over the pH range studied here. However, the influence of intermolecular resonant coupling is observed at lower pH. Specifically, at pH 2 the H_2O spectra are red shifted from the HOD spectra, which we attribute to stronger intermolecular resonant coupling in the former as at this pH these O-H oscillators point toward the bulk solution, forming symmetric hydrogen bonds with neighboring H_2O molecules as well as accepting a hydrogen from surface silanol sites.

ASSOCIATED CONTENT
Supporting Information

The following files are available free of charge via the Internet at https://pubs.acs.org. The file contains the effects of local field corrections of the vSFG SSP spectra for HOD in D_2O, vSFG PPP spectra collected as a function of the ionic strength, electrokinetic charge densities determined with the Grahame equation, error and $\chi^{(2)}$ phase from phase sensitive measurements, results of $\chi^{(2)}$ phase fit and the predicted phases over the ionic strength range, corresponding real component of the $\chi^{(2)}_{\text{total}}$ for HOD, information on the calculation of the g_3 term, and the determination of the $\chi^{(3)}$ spectra, comparison of the Stern and diffuse layer spectra at pH 12 to previous work.

AUTHOR INFORMATION
Corresponding Author

*E-mail: julianne.gibbs@ualberta.ca

Notes

The authors declare no competing financial interest.

ACKNOWLEDGEMENTS

REFERENCES

(1)   Gonella, G.; Backus, E. H. G.; Nagata, Y.; Bonthuis, D. J.; Loche, P.; Schlaich, A.; Netz, R. R.; Kühnle, A.; McCrum, I. T.; Koper, M. T. M.; Wolf, M.; Winter, B.; Meijer, G.; Campen, R. K.; Bonn, M. Water at Charged Interfaces. *Nat. Rev. Chem.* **2021**, *5* (7), 466–485. https://doi.org/10.1038/s41570-021-00293-2.

(2)   Peng, J.; Guo, J.; Ma, R.; Jiang, Y. Water-Solid Interfaces Probed by High-Resolution Atomic Force Microscopy. *Surf. Sci. Rep.* **2022**, *77* (1), 100549. https://doi.org/10.1016/j.surfrep.2021.100549.

(3)   Bourg, I. C.; Lee, S. S.; Fenter, P.; Tournassat, C. Stern Layer Structure and Energetics at Mica–Water Interfaces. *J. Phys. Chem. C* **2017**, *121* (17), 9402–9412. https://doi.org/10.1021/acs.jpcc.7b01828.

(4)   Brown, M. A.; Abbas, Z.; Kleibert, A.; Green, R. G.; Goel, A.; May, S.; Squires, T. M. Determination of Surface Potential and Electrical Double-Layer Structure at the Aqueous Electrolyte-Nanoparticle Interface. *Phys. Rev. X* **2016**, *6* (1), 011007. https://doi.org/10.1103/PhysRevX.6.011007.

(5)   Lützenkirchen, J.; Scharnweber, T.; Ho, T.; Striolo, A.; Sulpizi, M.; Abdelmonem, A. A Set-up for Simultaneous Measurement of Second Harmonic Generation and Streaming Potential and Some Test Applications. *J. Colloid Interface Sci.* **2018**, *529*, 294–305. https://doi.org/10.1016/j.jcis.2018.06.017.

(6)   Backus, E. H. G.; Schaefer, J.; Bonn, M. Probing the Mineral–Water Interface with Nonlinear Optical Spectroscopy. *Angew. Chem. Int. Ed.* **2021**, *60* (19), 10482–10501. https://doi.org/10.1002/anie.202003085.

(7)   Geiger, F. M. Second Harmonic Generation, Sum Frequency Generation, and χ(3): Dissecting Environmental Interfaces with a Nonlinear Optical Swiss Army Knife. *Annu. Rev. Phys. Chem.* **2009**, *60* (1), 61–83. https://doi.org/10.1146/annurev.physchem.59.032607.093651.

(8)   Covert, P. A.; Hore, D. K. Geochemical Insight from Nonlinear Optical Studies of Mineral–Water Interfaces. *Annu. Rev. Phys. Chem.* **2016**, *67* (1), 233–257. https://doi.org/10.1146/annurev-physchem-040215-112300.

(9)   Iler, R. K. *The Chemistry of Silica: Solubility, Polymerization, Colloid and Surface Properties, and Biochemistry*; Wiley: New York, 1979.

(10) Kosmulski, M. The PH Dependent Surface Charging and Points of Zero Charge. IX. Update. *Adv. Colloid Interface Sci.* **2021**, *296*, 102519. https://doi.org/10.1016/j.cis.2021.102519.

(11) Rehl, B.; Ma, E.; Parshotam, S.; DeWalt-Kerian, E. L.; Liu, T.; Geiger, F. M.; Gibbs, J. M. Water Structure in the Electrical Double Layer and the Contribution to the Total Interfacial Potential at Different Surface Charge Densities. *ChemRxiv*. https://doi.org/10.26434/chemrxiv-2022-p5fwp-v4.

(12)   Seki, T.; Yu, C.-C.; Chiang, K.-Y.; Tan, J.; Sun, S.; Ye, S.; Bonn, M.; Nagata, Y. Disentangling Sum-Frequency Generation Spectra of the Water Bending Mode at Charged Aqueous Interfaces. *J. Phys. Chem. B* **2021**, *125* (25), 7060–7067. https://doi.org/10.1021/acs.jpcb.1c03258.

(13)   Pezzotti, S.; Galimberti, D. R.; Shen, Y. R.; Gaigeot, M.-P. Structural Definition of the BIL and DL: A New Universal Methodology to Rationalize Non-Linear χ(2)(ω) SFG Signals at Charged Interfaces, Including χ(3)(ω) Contributions. *Phys. Chem. Chem. Phys.* **2018**, *20* (7), 5190–5199. https://doi.org/10.1039/C7CP06110B.

(14)   Wen, Y.-C.; Zha, S.; Liu, X.; Yang, S.; Guo, P.; Shi, G.; Fang, H.; Shen, Y. R.; Tian, C. Unveiling Microscopic Structures of Charged Water Interfaces by Surface-Specific Vibrational Spectroscopy. *Phys. Rev. Lett.* **2016**, *116* (1), 016101. https://doi.org/10.1103/PhysRevLett.116.016101.

(15)   Wang, H.; Xu, Q.; Liu, Z.; Tang, Y.; Wei, G.; Shen, Y. R.; Liu, W.-T. Gate-Controlled Sum-Frequency Vibrational Spectroscopy for Probing Charged Oxide/Water Interfaces. *J. Phys. Chem. Lett.* **2019**, *10* (19), 5943–5948. https://doi.org/10.1021/acs.jpclett.9b01908.

(16)   Urashima, S.; Myalitsin, A.; Nihonyanagi, S.; Tahara, T. The Topmost Water Structure at a Charged Silica/Aqueous Interface Revealed by Heterodyne-Detected Vibrational Sum Frequency Generation Spectroscopy. *J. Phys. Chem. Lett.* **2018**, *9* (14), 4109–4114. https://doi.org/10.1021/acs.jpclett.8b01650.

(17)   Jena, K. C.; Covert, P. A.; Hore, D. K. The Effect of Salt on the Water Structure at a Charged Solid Surface: Differentiating Second- and Third-Order Nonlinear Contributions. *J. Phys. Chem. Lett.* **2011**, *2* (9), 1056–1061. https://doi.org/10.1021/jz200251h.

(18)   Rehl, B.; Gibbs, J. M. Role of Ions on the Surface-Bound Water Structure at the Silica/Water Interface: Identifying the Spectral Signature of Stability. *J. Phys. Chem. Lett.* **2021**, *12* (11), 2854–2864. https://doi.org/10.1021/acs.jpclett.0c03565.

(19)   Sovago, M.; Campen, R. K.; Wurpel, G. W. H.; Müller, M.; Bakker, H. J.; Bonn, M. Vibrational Response of Hydrogen-Bonded Interfacial Water Is Dominated by Intramolecular Coupling. *Phys. Rev. Lett.* **2008**, *100* (17), 173901. https://doi.org/10.1103/PhysRevLett.100.173901.

(20)   Sovago, M.; Kramer Campen, R.; Bakker, H. J.; Bonn, M. Hydrogen Bonding Strength of Interfacial Water Determined with Surface Sum-Frequency Generation. *Chem. Phys. Lett.* **2009**, *470* (1), 7–12. https://doi.org/10.1016/j.cplett.2009.01.009.

(21)   Myalitsin, A.; Urashima, S.; Nihonyanagi, S.; Yamaguchi, S.; Tahara, T. Water Structure at the Buried Silica/Aqueous Interface Studied by Heterodyne-Detected Vibrational Sum-Frequency Generation. *J. Phys. Chem. C* **2016**, *120* (17), 9357–9363. https://doi.org/10.1021/acs.jpcc.6b03275.

(22)   Auer, B. M.; Skinner, J. L. IR and Raman Spectra of Liquid Water: Theory and Interpretation. *J. Chem. Phys.* **2008**, *128* (22), 224511. https://doi.org/10.1063/1.2925258.

(23)   Matt, S. M.; Ben-Amotz, D. Influence of Intermolecular Coupling on the Vibrational Spectrum of Water. *J. Phys. Chem. B* **2018**, *122* (21), 5375–5380. https://doi.org/10.1021/acs.jpcb.7b11063.

(24)   Cyran, J. D.; Backus, E. H. G.; Nagata, Y.; Bonn, M. Structure from Dynamics: Vibrational Dynamics of Interfacial Water as a Probe of Aqueous Heterogeneity. *J. Phys. Chem. B* **2018**, *122* (14), 3667–3679. https://doi.org/10.1021/acs.jpcb.7b10574.

(25) Schaefer, J.; Backus, E. H. G.; Nagata, Y.; Bonn, M. Both Inter- and Intramolecular Coupling of O–H Groups Determine the Vibrational Response of the Water/Air Interface. *J. Phys. Chem. Lett.* **2016**, *7* (22), 4591–4595. https://doi.org/10.1021/acs.jpclett.6b02513.

(26) Raymond, E. A.; Tarbuck, T. L.; Brown, M. G.; Richmond, G. L. Hydrogen-Bonding Interactions at the Vapor/Water Interface Investigated by Vibrational Sum-Frequency Spectroscopy of HOD/H2O/D2O Mixtures and Molecular Dynamics Simulations. *J. Phys. Chem. B* **2003**, *107* (2), 546–556. https://doi.org/10.1021/jp021366w.

(27) Stiopkin, I. V.; Weeraman, C.; Pieniazek, P. A.; Shalhout, F. Y.; Skinner, J. L.; Benderskii, A. V. Hydrogen Bonding at the Water Surface Revealed by Isotopic Dilution Spectroscopy. *Nature* **2011**, *474* (7350), 192–195. https://doi.org/10.1038/nature10173.

(28) Tian, C.-S.; Shen, Y. R. Isotopic Dilution Study of the Water/Vapor Interface by Phase-Sensitive Sum-Frequency Vibrational Spectroscopy. *J. Am. Chem. Soc.* **2009**, *131* (8), 2790–2791. https://doi.org/10.1021/ja809497y.

(29) Walker, D. S.; Richmond, G. L. Understanding the Effects of Hydrogen Bonding at the Vapor−Water Interface: Vibrational Sum Frequency Spectroscopy of H2O/HOD/D2O Mixtures Studied Using Molecular Dynamics Simulations. *J. Phys. Chem. C* **2007**, *111* (23), 8321–8330. https://doi.org/10.1021/jp070493v.

(30) Xu, X.; Shen, Y. R.; Tian, C. Phase-Sensitive Sum Frequency Vibrational Spectroscopic Study of Air/Water Interfaces: H2O, D2O, and Diluted Isotopic Mixtures. *J. Chem. Phys.* **2019**, *150* (14), 144701. https://doi.org/10.1063/1.5081135.

(31) Inoue, K. (井上賢一); Ahmed, M.; Nihonyanagi, S. (二本柳聡史); Tahara, T. (田原太平). Effect of Hydrogen-Bond on Ultrafast Spectral Diffusion Dynamics of Water at Charged Monolayer Interfaces. *J. Chem. Phys.* **2019**, *150* (5), 054705. https://doi.org/10.1063/1.5081077.

(32) Brown, M. A.; Goel, A.; Abbas, Z. Effect of Electrolyte Concentration on the Stern Layer Thickness at a Charged Interface. *Angew. Chem. Int. Ed.* **2016**, *55* (11), 3790–3794. https://doi.org/10.1002/anie.201512025.

(33) Tuladhar, A.; Dewan, S.; Pezzotti, S.; Brigiano, F. S.; Creazzo, F.; Gaigeot, M.-P.; Borguet, E. Ions Tune Interfacial Water Structure and Modulate Hydrophobic Interactions at Silica Surfaces. *J. Am. Chem. Soc.* **2020**, *142* (15), 6991–7000. https://doi.org/10.1021/jacs.9b13273.

(34) DeWalt-Kerian, E. L.; Kim, S.; Azam, Md. S.; Zeng, H.; Liu, Q.; Gibbs, J. M. PH-Dependent Inversion of Hofmeister Trends in the Water Structure of the Electrical Double Layer. *J. Phys. Chem. Lett.* **2017**, *8* (13), 2855–2861. https://doi.org/10.1021/acs.jpclett.7b01005.

(35) Darlington, A. M.; Jarisz, T. A.; DeWalt-Kerian, E. L.; Roy, S.; Kim, S.; Azam, Md. S.; Hore, D. K.; Gibbs, J. M. Separating the PH-Dependent Behavior of Water in the Stern and Diffuse Layers with Varying Salt Concentration. *J. Phys. Chem. C* **2017**, *121* (37), 20229–20241. https://doi.org/10.1021/acs.jpcc.7b03522.

(36) Glasoe, P. K.; Long, F. A. Use of Glass Electrodes to Measure Acidities in Deuterium Oxide. *J. Phys. Chem.* **1960**, *64* (1), 188–190. https://doi.org/10.1021/j100830a521.

(37) Krężel, A.; Bal, W. A Formula for Correlating PKa Values Determined in D2O and H2O. *J. Inorg. Biochem.* **2004**, *98* (1), 161–166. https://doi.org/10.1016/j.jinorgbio.2003.10.001.

(38) Luxbacher, Thomas. *The Zeta Potential for Solid Surface Analysis - A Practical Guide to Streaming Potential Measurement*; Anton Paar GmbH: Austria, 2014.

(39) Hardy, R. C.; Cottington, R. L. Viscosity of Deuterium Oxide and Water from 5° to 125°C. *J. Chem. Phys.* **1949**, *17* (5), 509–510. https://doi.org/10.1063/1.1747310.

(40) Horita, J.; Cole, D. R. Stable Isotope Partitioning in Aqueous and Hydrothermal Systems to Elevated Temperatures. *Aqueous Syst. Elev. Temp. Press. Phys. Chem. Water Steam Hydrothermal Solut.* **2004**, 277–319. https://doi.org/10.1016/B978-012544461-3/50010-7.

(41) Vidulich, G. A.; Evans, D. F.; Kay, R. L. The Dielectric Constant of Water and Heavy Water between 0 and 40.Degree. *J. Phys. Chem.* **1967**, *71* (3), 656–662. https://doi.org/10.1021/j100862a028.

(42) Sovago, M.; Vartiainen, E.; Bonn, M. Erratum: "Observation of Buried Water Molecules in Phospholipid Membranes by Surface Sum-Frequency Generation Spectroscopy" [J. Chem. Phys. 131, 161107 (2009)]. *J. Chem. Phys.* **2010**, *133* (22), 229901. https://doi.org/10.1063/1.3511705.

(43) Sovago, M.; Vartiainen, E.; Bonn, M. Determining Absolute Molecular Orientation at Interfaces: A Phase Retrieval Approach for Sum Frequency Generation Spectroscopy. *J. Phys. Chem. C* **2009**, *113* (15), 6100–6106. https://doi.org/10.1021/jp810123g.

(44) Sovago, M.; Vartiainen, E.; Bonn, M. Observation of Buried Water Molecules in Phospholipid Membranes by Surface Sum-Frequency Generation Spectroscopy. *J. Chem. Phys.* **2009**, *131* (16), 161107. https://doi.org/10.1063/1.3257600.

(45) Lambert, A. G.; Davies, P. B.; Neivandt, D. J. Implementing the Theory of Sum Frequency Generation Vibrational Spectroscopy: A Tutorial Review. *Appl. Spectrosc. Rev.* **2005**, *40* (2), 103–145. https://doi.org/10.1081/ASR-200038326.

(46) Hore, D. K.; Tyrode, E. Probing Charged Aqueous Interfaces Near Critical Angles: Effect of Varying Coherence Length. *J. Phys. Chem. C* **2019**, *123* (27), 16911–16920. https://doi.org/10.1021/acs.jpcc.9b05256.

(47) Cai, C.; Azam, Md. S.; Hore, D. K. Determining the Surface Potential of Charged Aqueous Interfaces Using Nonlinear Optical Methods. *J. Phys. Chem. C* **2021**, *125* (45), 25307–25315. https://doi.org/10.1021/acs.jpcc.1c07761.

(48) Rehl, B.; Rashwan, M.; DeWalt-Kerian, E. L.; Jarisz, T. A.; Darlington, A. M.; Hore, D. K.; Gibbs, J. M. New Insights into χ(3) Measurements: Comparing Nonresonant Second Harmonic Generation and Resonant Sum Frequency Generation at the Silica/Aqueous Electrolyte Interface. *J. Phys. Chem. C* **2019**, *123* (17), 10991–11000. https://doi.org/10.1021/acs.jpcc.9b01300.

(49) Eftekhari-Bafrooei, A.; Borguet, E. Effect of Hydrogen-Bond Strength on the Vibrational Relaxation of Interfacial Water. *J. Am. Chem. Soc.* **2010**, *132* (11), 3756–3761. https://doi.org/10.1021/ja907745r.

(50) Schaefer, J.; Gonella, G.; Bonn, M.; G. Backus, E. H. Surface-Specific Vibrational Spectroscopy of the Water/Silica Interface: Screening and Interference. *Phys. Chem. Chem. Phys.* **2017**, *19* (25), 16875–16880. https://doi.org/10.1039/C7CP02251D.

(51) Gonella, G.; Lütgebaucks, C.; de Beer, A. G. F.; Roke, S. Second Harmonic and Sum-Frequency Generation from Aqueous Interfaces Is Modulated by Interference. *J. Phys. Chem. C* **2016**, *120* (17), 9165–9173. https://doi.org/10.1021/acs.jpcc.5b12453.

(52) Grahame, D. C. The Electrical Double Layer and the Theory of Electrocapillarity. *Chem. Rev.* **1947**, *41* (3), 441–501. https://doi.org/10.1021/cr60130a002.

(53) Dedic, J.; Okur, H. I.; Roke, S. Polyelectrolytes Induce Water-Water Correlations That Result in Dramatic Viscosity Changes and Nuclear Quantum Effects. *Sci. Adv.* **2019**, *5* (12), eaay1443. https://doi.org/10.1126/sciadv.aay1443.

(54) de Beer, A. G. F.; Chen, Y.; Scheu, R.; Conboy, J. C.; Roke, S. Analysis of Complex Spectra Using Fourier Filtering. *J. Phys. Chem. C* **2013**, *117* (50), 26582–26587. https://doi.org/10.1021/jp406161n.

(55) de Beer, A. G. F.; Samson, J.-S.; Hua, W.; Huang, Z.; Chen, X.; Allen, H. C.; Roke, S. Direct Comparison of Phase-Sensitive Vibrational Sum Frequency Generation with Maximum Entropy Method: Case Study of Water. *J. Chem. Phys.* **2011**, *135* (22), 224701. https://doi.org/10.1063/1.3662469.

(56) Hofmann, M. J.; Koelsch, P. Retrieval of Complex χ(2) Parts for Quantitative Analysis of Sum-Frequency Generation Intensity Spectra. *J. Chem. Phys.* **2015**, *143* (13), 134112. https://doi.org/10.1063/1.4932180.

(57) Johansson, P. K.; Koelsch, P. Vibrational Sum-Frequency Scattering for Detailed Studies of Collagen Fibers in Aqueous Environments. *J. Am. Chem. Soc.* **2014**, *136* (39), 13598–13601. https://doi.org/10.1021/ja508190d.

(58) Roy, S.; Covert, P. A.; Jarisz, T. A.; Chan, C.; Hore, D. K. Surface–Bulk Vibrational Correlation Spectroscopy. *Anal. Chem.* **2016**, *88* (9), 4682–4691. https://doi.org/10.1021/acs.analchem.5b04544.

(59) Yang, P.-K.; Huang, J. Y. Model-Independent Maximum-Entropy Method for the Analysis of Sum-Frequency Vibrational Spectroscopy. *J. Opt. Soc. Am. B* **2000**, *17* (7), 1216. https://doi.org/10.1364/JOSAB.17.001216.

(60) Yang, W.-C.; Hore, D. K. Broadband Models and Their Consequences on Line Shape Analysis in Vibrational Sum-Frequency Spectroscopy. *J. Chem. Phys.* **2018**, *149* (17), 174703. https://doi.org/10.1063/1.5053128.

(61) Ma, E.; Ohno, P. E.; Kim, J.; Liu, Y.; Lozier, E. H.; Miller, T. F.; Wang, H.-F.; Geiger, F. M. A New Imaginary Term in the Second-Order Nonlinear Susceptibility from Charged Interfaces. *J. Phys. Chem. Lett.* **2021**, *12* (24), 5649–5659. https://doi.org/10.1021/acs.jpclett.1c01103.

(62) Ohno, P. E.; Chang, H.; Spencer, A. P.; Liu, Y.; Boamah, M. D.; Wang, H.; Geiger, F. M. Beyond the Gouy–Chapman Model with Heterodyne-Detected Second Harmonic Generation. *J. Phys. Chem. Lett.* **2019**, *10* (10), 2328–2334. https://doi.org/10.1021/acs.jpclett.9b00727.

(63) Morita, A.; Hynes, J. T. A Theoretical Analysis of the Sum Frequency Generation Spectrum of the Water Surface. *Chem. Phys.* **2000**, *258* (2), 371–390. https://doi.org/10.1016/S0301-0104(00)00127-0.

(64) Cyran, J. D.; Donovan, M. A.; Vollmer, D.; Brigiano, F. S.; Pezzotti, S.; Galimberti, D. R.; Gaigeot, M.-P.; Bonn, M.; Backus, E. H. G. Molecular Hydrophobicity at a Macroscopically Hydrophilic Surface. *Proc. Natl. Acad. Sci.* **2019**, *116* (5), 1520–1525. https://doi.org/10.1073/pnas.1819000116.

(65) Dalstein, L.; Potapova, E.; Tyrode, E. The Elusive Silica/Water Interface: Isolated Silanols under Water as Revealed by Vibrational Sum Frequency Spectroscopy. *Phys. Chem. Chem. Phys.* **2017**, *19* (16), 10343–10349. https://doi.org/10.1039/C7CP01507K.

(66) Kaliannan, N. K.; Henao Aristizabal, A.; Wiebeler, H.; Zysk, F.; Ohto, T.; Nagata, Y.; Kühne, T. D. Impact of Intermolecular Vibrational Coupling Effects on the Sum-Frequency Generation Spectra of the Water/Air Interface. *Mol. Phys.* **2020**, *118* (4), 1620358. https://doi.org/10.1080/00268976.2019.1620358.

(67)   Moberg, D. R.; Straight, S. C.; Paesani, F. Temperature Dependence of the Air/Water Interface Revealed by Polarization Sensitive Sum-Frequency Generation Spectroscopy. *J. Phys. Chem. B* **2018**, *122* (15), 4356–4365. https://doi.org/10.1021/acs.jpcb.8b01726.